High temperature crystal structures and superionic properties of SrCl$_2$, SrBr$_2$, BaCl$_2$ and BaBr$_2$

Stephen Hull [a,*], Stefan T. Norberg [a,b], Istaq Ahmed [b], Sten G. Eriksson [b], Chris E. Mohn [c]

[a] The ISIS Facility, STFC Rutherford Appleton Laboratory, Chilton, Didcot, Oxfordshire OX11 0QX, United Kingdom
[b] Department of Chemical and Biological Engineering, Chalmers University of Technology, SE-412 96 Gothenburg, Sweden
[c] Department of Chemistry and Centre for Materials Science and Nanotechnology, University of Oslo, P.O. Box 1033 Blindern, N-0315 Oslo, Norway

ARTICLE INFO

Received 16 June 2011
Received in revised form
1 September 2011
Accepted 4 September 2011
Available online 10 September 2011

Keywords:
Superionic conduction
Alkaline-earth halides
Neutron diffraction
Phase transitions
Fluorite structure

ABSTRACT

The structural properties of the binary alkaline-earth halides SrCl$_2$, SrBr$_2$, BaCl$_2$ and BaBr$_2$ have been investigated from ambient temperature up to close to their melting points, using the neutron powder diffraction technique. Fluorite-structured SrCl$_2$ undergoes a gradual transition to a superionic phase at 900–1100 K, characterised by an increasing concentration of anion Frenkel defects. At a temperature of 920(3) K, the tetragonal phase of SrBr$_2$ undergoes a first-order transition to a cubic fluorite phase. This high temperature phase shows the presence of extensive disorder within the anion sublattice, which differs from that found in superionic SrCl$_2$. BaCl$_2$ and BaBr$_2$ both adopt the cotunnite crystal structure under ambient conditions. BaCl$_2$ undergoes a first-order structural transition at 917(5) K to a disordered fluorite-structured phase. The relationship between the (disordered) crystal structures and the ionic conductivity behaviour is discussed and the influence of the size of the mobile anion on the superionic behaviour is explored.

© 2011 Elsevier Inc. All rights reserved.

1. Introduction

The temperature dependence of the crystal structures of compounds of composition AX_2, where $A=$ Ca^{2+}, Sr^{2+}, Ba^{2+} and Pb^{2+} and $X=$ F$^-$, Cl$^-$ and Br$^-$, have been extensively studied using a variety of experimental and computational techniques, with particular interest focussed on CaF$_2$, SrF$_2$, BaF$_2$, β-PbF$_2$ and SrCl$_2$ because, on heating, they undergo a broad transition to a superionic phase characterised by a very high anionic conductivity (comparable to the molten state, see Fig. 1a for the case of SrCl$_2$) [1–8]. All five compounds adopt the cubic fluorite crystal structure (space group $Fm\overline{3}m$, $Z=4$, $a\sim5.4$–7.0 Å) in which the cations and anions are located on the $4(a)$ 0,0,0 and $8(c)$ $\frac{1}{4},\frac{1}{4},\frac{1}{4}$ sites, respectively. The ionic arrangement can be described as a face centred cubic (f.c.c.) array of A^{2+} cations in which the X^- anions sit in all the tetrahedral interstices or, as shown in Fig. 2a, as a three-dimensional arrangement of edge-sharing AX_8 cubes.
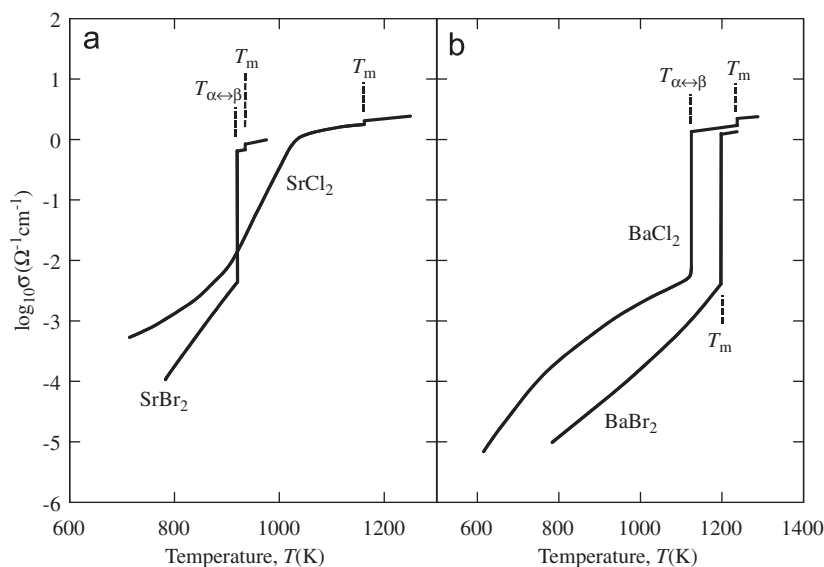
Neutron diffraction studies initially proposed that the increase in ionic conductivity of the fluorite-structured halides is associated with the formation of thermally induced anion-Frenkel defects in which the interstitial X^- is located in the octahedral $4(b)$ $\frac{1}{2},\frac{1}{2},\frac{1}{2}$ interstices within the f.c.c. A^{2+} sublattice (labelled $X4$ in Fig. 2b), which are the centres of the empty anion cubes in Fig. 2a [9]. However, subsequent studies [10], including analysis of the coherent diffuse scattering collected from single crystals of CaF$_2$, β-PbF$_2$ and SrCl$_2$ [11], showed that these sites are not appreciably occupied within the highly conducting phase and, instead, the preferred site for the interstitial anions is in the $48(g)$ $\frac{1}{2},y,y$, $y\sim0.38$ positions, which lie between the cube centre and midpoint of a cube edge (labelled $X2$ in Fig. 2b). The presence of these interstitials causes the two nearest neighbour anions to relax away from the interstitial into surrounding empty cubes ($32(f)$ x,x,x sites with $x\sim0.40$, shown as the $X3$ sites in Fig. 2b), leading to the anion-Frenkel defect model shown in Fig. 2c (with the anion interstitial and relaxed nearest neighbours labelled X_I and X_R, respectively). Quasielastic neutron scattering studies indicated that these defects have a typical lifetime of $\sim10^{-12}$ s [11], whilst their stability was determined by static energy calculations [12].

Turning to the other members of the AX_2 ($A=$ Ca^{2+}, Sr^{2+}, Ba^{2+} and Pb^{2+}; $X=$ F$^-$, Cl$^-$ and Br$^-$) family of compounds, CaCl$_2$ and CaBr$_2$ both adopt an orthorhombically distorted version of the rutile structure (space group $Pnnm$, $Z=4$) and undergo a continuous transition to the tetragonal rutile form (space group $P4_2/mnm$, $Z=2$) at temperatures of 508 K and 826 K, respectively [13,14]. Neither compound shows high ionic conductivity prior to melting [5]. BaCl$_2$, PbCl$_2$, BaBr$_2$ and PbBr$_2$ all adopt the orthorhombic cotunnite structure (space group $Pnma$, $Z=4$) under ambient conditions [15], which can be described as a hexagonal close packed (h.c.p.) array of A^{2+} cations with all the tetrahedral

  E-mail address: stephen.hull@stfc.ac.uk (S. Hull).

0022-4596/$ - see front matter © 2011 Elsevier Inc. All rights reserved.
doi:10.1016/j.jssc.2011.09.004

Fig. 1. The temperature dependence of the ionic conductivity, $\log_{10}\sigma$, for (a) $SrCl_2$ and $SrBr_2$ and (b) $BaCl_2$ and $BaBr_2$ (after [5,20]).
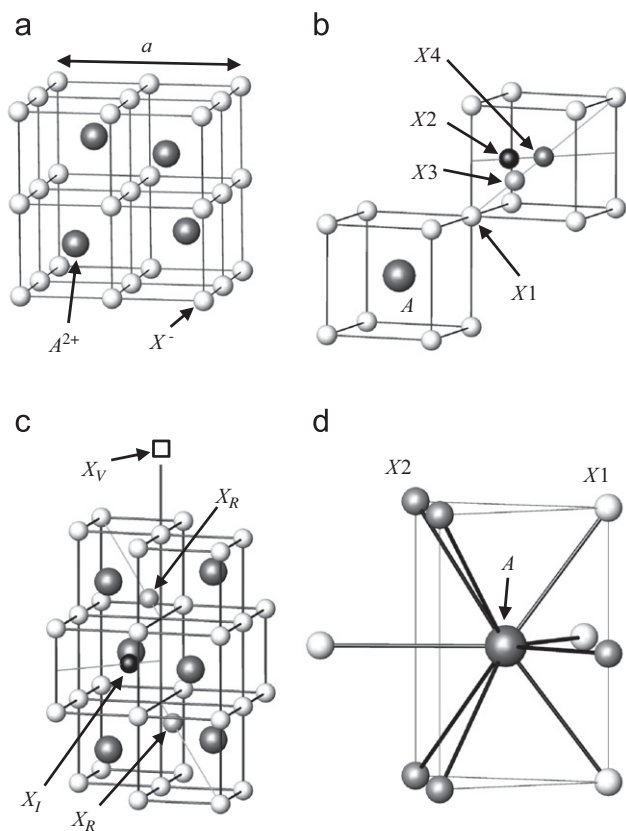
Fig. 2. (a) The cubic fluorite crystal structure of a compound of stoichiometry AX_2, with the A^{2+} cations occupying alternate cube centres within a simple cubic array of X^- anions. The cubic lattice parameter a is shown. (b) The anion sites proposed to be occupied within anion disordered halide and oxide fluorites (after [7]). (c) The anion-Frenkel defect proposed to occur within the superionic phase of the halide fluorites [11,12]. X_V, X_I and X_R denote an anion vacancy, anion interstitial and relaxed anions, respectively. (d) The anion co-ordination surrounding a cation within a cotunnite-structured compound of stoichiometry AX_2.

interstices occupied by two symmetry independent X^- anions. However, all the ions are displaced away from the idealised positions by significant distances, leading to a more irregular arrangement in which the A^{2+} cations are surrounded by a total of nine X^- in the form of a distorted tricapped trigonal

prism (see Fig. 2d). As a consequence of the higher co-ordination, the cotunnite structure is more densely packed than the fluorite one, and several fluorite-structured compounds transform to a cotunnite phase at elevated pressures, including BaF_2 [16], $SrCl_2$ [17] and PbF_2 [17–19]. In the case of PbF_2, the cotunnite (α) form can be retained under ambient conditions, but transforms to the fluorite-structured (β) phase on heating above ~ 610 K [18]. Measurements of the ionic conductivity indicate that both $BaCl_2$ and $PbCl_2$ show high ionic conductivities in narrow temperature ranges just below their melting points (see [20] and [21], respectively, and the former is illustrated in Fig. 1b). Heat capacity measurements of $BaCl_2$ also show the presence of a phase transition at 1193 K, prior to melting at 1233 K [22], though no structural details have been presented for the high temperature phase.

The final compound in this family, $SrBr_2$, was originally proposed to adopt the cotunnite structure on the basis of X-ray single crystal diffraction data [23]. However, this reported structure contains Sr–Br distances significantly longer than the sum of the ionic radii and led to a redetermination of the structure using X-ray powder diffraction methods [24]. $SrBr_2$ was shown to adopt a larger tetragonal unit cell (space group $P4/n$, $Z=10$) [25], isostructural with $EuBr_2$ [26] and USe_2 [27]. Drop calorimetry studies showed that $SrBr_2$ undergoes a solid–solid phase transition at a temperature of 918 K, prior to melting at 930 K [22], with later studies reporting temperatures of 919 K and 928 K [28] or 915 K and 922 K [29], respectively. The solid–solid transition was found to possess a higher entropy than the melting transition (13.2 J K^{-1} mol^{-1}, compared to 11.3 J K^{-1} mol^{-1} [22]), which implies the presence of significant disorder within the high temperature phase. This observation was supported by the subsequent report of an abrupt increase of over two orders of magnitude in the ionic conductivity of $SrBr_2$ at the transition (see Fig. 1a), to a value of around 1 Ω^{-1} cm^{-1} which is only slightly lower than that found above the melting point [20].

In this paper we report the results of a powder neutron diffraction study of $SrCl_2$, $SrBr_2$, $BaCl_2$ and $BaBr_2$ from ambient temperatures up to close to their melting points. In comparison to the other binary AX_2 halides, the structural properties of these compounds are rather poorly understood. This allows a detailed discussion of the effects of temperature on the crystal structures, including the nature of the extensive anion disorder which characterises the superionic phases of $SrCl_2$, $SrBr_2$ and $BaCl_2$ in the temperature ranges immediately below their melting points

(see Fig. 1) and permits a discussion of the role of anion size on the nature of the ionic defects and their diffusion mechanisms in binary alkaline-earth halides.

2. Experimental details

Polycrystalline samples were supplied by the Sigma Aldrich chemical company and of stated purity 99.995% ($SrCl_2$ and $SrBr_2$) and 99.999% ($BaCl_2$ and $BaBr_2$). After drying, the powders were loaded into a silica glass ampoule of 0.25 mm wall thickness, outer diameter 7 mm and length 50 mm in a glove box under an inert atmosphere, prior to sealing under vacuum. The experiments were performed on the Polaris powder diffractometer at the ISIS facility, U.K. [30], with the sealed silica ampoules housed within a thin-walled (40 μm) vanadium can of ~11 mm diameter. Diffraction data were collected at 39 temperatures for $SrCl_2$ (up to $T_{max}=1113(1)$ K, where the melting temperature $T_m=1146$ K [22]), at 40 temperatures for $SrBr_2$ ($T_{max}=926(1)$ K, $T_m=930$ K [22]), at 24 temperatures for $BaCl_2$ ($T_{max}=1223(1)$ K, $T_m=1233$ K [22]) and at 39 temperatures for $BaBr_2$ ($T_{max}=1114$ (1) K, $T_m=1130$ K [22]). Temperature measurement was achieved using a type-K thermocouple in contact with the vanadium sample can. Diffraction data were collected using the backscattering detector bank which covers the scattering angles $130° < 2\theta < 160°$ (providing data over the d-spacing range $0.2 < d(Å) < 3.2$ with a resolution $\Delta d/d \sim 5 \times 10^{-3}$) and the low-angle detector bank situated at $28° < 2\theta < 42°$ (providing data over the d-spacing range $0.5 < d(Å) < 8.3$ with a resolution of $\Delta d/d \sim 10^{-2}$). Rietveld refinement of the powder diffraction data only used the former data (with typical spectra given in the supplementary material (Suppl. 1) to illustrate its statistical quality) and the analysis program GSAS [31]. The quality of the fits using different structural models was assessed using the conventional χ^2 statistic, defined by

$$\chi^2 = \sum_{N_d} \frac{(I_{obs}-I_{calc})^2}{(\sigma I_{obs})^2} / (N_d - N_v), \tag{1}$$

where N_d is the number of data points used in the fit and N_v is the number of fitted variables. I_{obs} and I_{calc} are the observed and calculated intensities, respectively, and σI_{obs} is the estimated standard deviation on I_{obs}, derived from the counting statistics.

3. Results and discussion

The results of the neutron powder diffraction studies are presented in the following section in the order $SrCl_2$, $SrBr_2$, $BaCl_2$ and $BaBr_2$. By analogy with the case of PbF_2, low temperature and high temperature phases are labelled α and β, respectively.

3.1. Superionic transition in $SrCl_2$

The neutron diffraction data collected from $SrCl_2$ at an ambient temperature of 298(1) K could be successfully fitted ($\chi^2=1.12$) with the accepted model of a ordered cubic fluorite crystal structure. In the fitting procedure, a total of 18 variable parameters were used, comprising a scale factor, the cubic lattice parameter, isotropic thermal vibration parameters for each ionic species, four parameters describing Gaussian and Lorentzian contributions to the instrumental peakshape and 10 coefficients of a shifted Chebyshev polynomial function used to describe the background scattering. The structural parameters derived under ambient conditions were used as the starting model for the analysis of the diffraction data collected at the first temperature on heating, and this process continued iteratively for the datasets

measured on increasing temperature. The ordered fluorite structural model provided good fits to the experimental diffraction data collected at temperatures up to around 1000 K. At higher temperatures, gradual changes in the relative intensities of some of the Bragg peaks lead to progressively poorer fits. This temperature range corresponds to the superionic phase of $SrCl_2$ (for which the superionic transition temperature, defined by the peak in the specific heat, C_p, has been reported to occur at $T_c=1001$ K [32] or $T_c=1003$ K [22]) and, following the previous diffraction studies [9–11], indicate the onset of dynamic anion disorder associated with the gradual transition to a superionic phase.

Analysis of the structure of the superionic phase of $SrCl_2$ used neutron powder diffraction data collected at a temperature of 1073(1) K and employed a number of different structural models to describe the nature of the dynamic ionic disorder. The simplest structural description (model I) is the ordered fluorite arrangement, with full occupancy of both cation and anion sites. As discussed above, this gives a relatively poor fit to the experimental data, with $\chi^2=4.21$. The second model allows the possibility of anion disorder in a crude manner, by allowing the occupancy of the lattice anion site to vary. A significant reduction in both χ^2 (to 2.18) and the Cl^- occupancy (to ~0.75) support the presence of extensive anion disorder, but is physically unrealistic because the structural description does not specify the locations of the displaced anions. The preferred locations for anions within fluorite-structured compounds have been extensively studied, including both halide and oxide compounds, and for systems showing both intrinsic (thermally induced Frenkel) and extrinsic (induced by chemical doping) disorder (for further details and references, see [7]). As illustrated in Fig. 2b, the positions most commonly occupied within a fluorite-structured compound of stoichiometry AX_2 are the $X2$ (48(g) $\frac{1}{2}$,y,y sites with $y \sim 0.38$), $X3$ (32(f) x,x,x sites with $x \sim 0.40$) and $X4$ (4(b) $\frac{1}{2}$,$\frac{1}{2}$,$\frac{1}{2}$ sites) positions. The label $X1$ is used to denote the lattice 8(c) sites at $\frac{1}{4}$,$\frac{1}{4}$,$\frac{1}{4}$, etc. and, for the case of $SrCl_2$, $X=Cl$.

The extensive dynamic disorder within the superionic phase of $SrCl_2$ causes a rapid fall-off in the intensities of the Bragg peaks with decreasing d-spacings and, in view of the relatively small number of observed reflections, it is not feasible to determine the preferred occupancy of the $X1$–$X4$ sites by including all four simultaneously and allowing the relative populations of each to vary. Instead, we consider each in turn and include one, or at most two, sites within specific structural models. In all cases, the total occupancy of the anion sites is constrained to equal that given by the stoichiometry and additional fitted parameters comprised a scale factor, the cubic lattice parameter, any positional parameters allowed to vary by the symmetry (y_{Cl2} and x_{Cl3}), isotropic thermal vibration parameters, four parameters describing Gaussian and Lorentzian contributions to the instrumental peakshape and 15 coefficients of a shifted Chebyshev polynomial function used to describe the background scattering.

Allowing the anions displaced from their lattice Cl1 sites to occupy the Cl2 (model III) and Cl3 (model IV) sites both gave a slight improvement in the quality of the fit (to $\chi^2=1.73$ and $\chi^2=1.66$, respectively), with stable refinement of the positional parameters provided that the isotropic thermal parameters of the two anion sites were constrained to remain equal. By contrast, use of the Cl4 sites (model V) gave a poorer fit with an unphysical occupancy (i.e. > 1) of these positions. The final structural model (model VI) describes the dynamic Frenkel defects illustrated in Fig. 2c, with the interstitial and relaxed nearest neighbour Cl^- occupying the Cl2 and Cl3 positions, respectively, and their site occupancies constrained to remain in the ratio 1:2. This model provided the best fit to the experimental data, with $\chi^2=1.28$, though it was necessary to constrain the isotropic thermal parameters of the Cl2 and Cl3 sites to be equal in order to achieve

a stable minimum. A number of other structural models were considered, including other combinations of the Cl2, Cl3 and Cl4 sites, but all led to unstable refinement and/or physically meaningless fitted parameters.

The success of model VI is consistent with the neutron single crystal diffraction study of superionic SrCl$_2$ [11] and the quality of the final fit to the experimental data collected at 1073(1) K is illustrated in Fig. 3a. The fitted parameters are listed in Table 1, together with details of the goodness-of-fit parameters. Finally, in order to determine the temperature dependence of the anion-Frenkel disorder, the structural model for SrCl$_2$ obtained at a temperature of 1073(1) K was used to fit the experimental data collected at all temperatures (though with the positional parameters y_{Cl2} and x_{Cl3} fixed at the values obtained at 1073(1) K). The resultant parameters are listed in the supplementary material (Suppl. 2). As illustrated in Fig. 4, there is a marked increase in the concentration, n_V, of vacancies on the lattice anion site (where, with reference to Table 1, $n_V = 1 - m_{Cl1}/8$ and m_{Cl1} is the number of anions per unit cell occupying the Cl1 positions) at temperatures above around 1000 K, consistent with the onset of superionic conduction. As illustrated in Fig. 5a, the superionic transition is also associated with an anomalous increase in the thermal expansion, as observed previously for other fluorite-structured superionic halides [33–35].
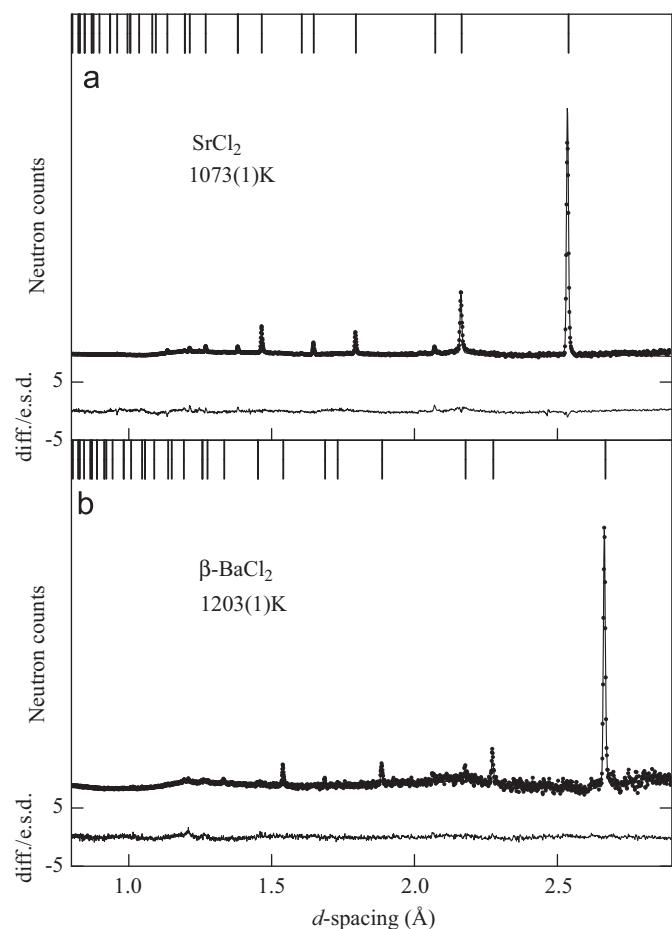
Fig. 3. The least-squares fits to the powder neutron diffraction data collected from superionic (a) SrCl$_2$ at 1073(1) K and (b) β-BaCl$_2$ at 1203(1) K. The dots are the experimental data points (with the background from the silica sample container and furnace subtracted) and the solid lines are the calculated profiles using the parameters listed in Table 1. The lower traces show the difference (measured minus calculated) divided by the estimated standard deviation on the experimental data points. The rows of tick marks along the top of the figures denote the calculated positions of all the symmetry allowed Bragg reflections for space group $Fm\overline{3}m$.

3.2. Crystal structure of α-SrBr$_2$

The crystal structure of α-SrBr$_2$ under ambient conditions was investigated using the neutron powder diffraction data collected at 291(1) K. The d-spacings of the observed reflections and the extinction conditions ($h\,k\,0$, $h+k=2n$; $h\,0\,0$, $h=2n$) are consistent with the previously proposed tetragonal unit cell ($a \sim 11.6$ Å and $c \sim 7.2$ Å) and $P4/n$ symmetry [24,25]. As a consequence, analysis of the diffraction data started using the most recently reported structural model [25], which has the cations located on two sites, Sr1 in the general 8(g) $x_{Sr1}, y_{Sr1}, z_{Sr1}$ positions and Sr2 in the 2(c) sites at $\frac{1}{4}, \frac{1}{4}, z_{Sr2}$. The 20 anions per unit cell sit on two sets of 8(g) sites, Br1 at $x_{Br1}, y_{Br1}, z_{Br1}$ and Br2 at $x_{Br2}, y_{Br2}, z_{Br2}$, plus the 2($a$) and 2($b$) sites at $\frac{1}{4}, \frac{3}{4}, 0$ and $\frac{1}{4}, \frac{3}{4}, \frac{1}{2}$, respectively. A total of 33 variable parameters were used in the final fitting procedure, comprising a scale factor, two lattice parameters, 10 positional parameters ($x_{Sr1}, y_{Sr1}, z_{Sr1}, z_{Sr2}, x_{Br1}, y_{Br1}, z_{Br1}, x_{Br2}, y_{Br2}$ and z_{Br2}), six isotropic thermal vibration parameters ($u_{Sr1}, u_{Sr2}, u_{Br1}, u_{Br2}, u_{Br3}$ and u_{Br4}), four parameters describing Gaussian and Lorentzian contributions to the instrumental peakshape and 10 coefficients of a shifted Chebyshev polynomial function used to describe the background scattering. The quality of the final fit ($\chi^2 = 1.26$) is illustrated in Fig. 6a, with the final fitted parameters listed in Table 2. Attempts to refine anisotropic thermal vibration parameters required a large number (18) of additional variables and proved unsuccessful, with several of the ellipsoids being non positive definite.

The ionic arrangement within the α-SrBr$_2$ phase is rather unusual and it is interesting to consider its crystal structure in some detail. The bond lengths between the Sr^{2+} and Br$^-$ are listed in Table 3, together with the Br$^-$–Sr^{2+}–Br$^-$ bond angles. The anion co-ordination around both the Sr1 and Sr2 is eightfold and can be described as a distorted square antiprism, with the former surrounded by three Br1, three Br2, one Br3 and one Br4 anions and the latter co-ordinated to four Br1 and four Br2 anions. As shown in Fig. 7a and b, the degree of distortion is significantly greater in the former case, with seven of the distances in the range 3.093(4) Å to 3.263(3) Å but an eighth (to a Br1) somewhat further away at 3.597(3) Å. By contrast, all the eight anion contacts around the Sr2 cations are in the range of 3.135(3)–3.160(3) Å. The Sr1Br$_8$ and Sr2Br$_8$ polyhedra are connected via common triangular faces comprising two Br1 and a single Br2 (Fig. 7c). All the Br$^-$ are surrounded by four cations in the form of a tetrahedron. The Br1 and Br2 sites are both surrounded by three Sr1 and one Sr2, whilst both the Br3 and Br4 positions are bonded to four Sr1 cations. The longer Sr1–Br1 distance mentioned above means that the Br1 centred tetrahedra are rather distorted (Sr^{2+}–Br$^-$–Sr^{2+} angles in the range of 86.05(7)–151.9(1)°, rather than the ideal value of $2\sin^{-1}\sqrt{2/3} = 109.47°$), whilst those surrounding Br2 are slightly less distorted (93.86(9)° to 138.7(1)°) and the Br3 and Br4 centred polyhedra are virtually perfect (109.19(5)° to 110.04(9)° and 109.37(5)° to 109.7(1)°, respectively).

3.3. Relationship between the α-SrBr$_2$ and fluorite crystal structures

On the basis of the Sr^{2+} and Br$^-$ bond lengths listed in Table 3, the average Sr^{2+}–Br$^-$ distance of ≈ 3.18 Å predicts that a fluorite-structured form of SrBr$_2$ would be expected to possess a cubic lattice parameter of $a_f \sim 7.34$ Å, where the subscript 'f' denotes 'fluorite'. As discussed previously for the case of USe$_2$ [27] (which is isostructural with α-SrBr$_2$), the unit cell parameters of the tetragonal unit cell, a_β and c_β, imply a relationship between the two phases of $a_\alpha = b_\alpha = \sqrt{(5/2)}a_f$ and $c_\alpha = a_f$, which corresponds to a rotation of the principal axes in the (0 0 1) plane of $\tan^{-1}(1/3) = 18.43°$ (see Fig. 8). Under these circumstances, the value of c_α/a_α would be $\sqrt{2/5} = 0.63246$, whereas the observed

Table 1
Summary of the results of the least-squares refinements of the neutron powder diffraction data collected from anion disordered, fluorite-structured SrCl$_2$, β-SrBr$_2$ and β-BaCl$_2$.

Phase	SrCl$_2$	β-SrBr$_2$	β-BaCl$_2$
Temperature (K)	$T=1073(1)$	$T=926(1)$	$T=1203(1)$
Space group	$Fm\overline{3}m$	$Fm\overline{3}m$	$Fm\overline{3}m$
Lattice parameter (Å)	$a=7.1806(2)$	$a=7.54078(5)$	$a=7.5469(4)$
Unit cell volume (Å^3)	$V=370.23(1)$	$V=428.795(5)$	$V=429.84(4)$
Volume per formula unit (Å^3)	$V/Z=92.558(4)$	$V/Z=107.199(1)$	$V/Z=107.46(1)$
Model I (ordered fluorite)	$\chi^2=4.21$	$\chi^2=5.37$	$\chi^2=2.17$
Model II (anion vacancies)	$\chi^2=2.18$	$\chi^2=2.44$	$\chi^2=1.66$
Model III ($X1$ and $X2$)	$\chi^2=1.73$	$\underline{\chi^2=1.28}$	$\chi^2=1.31$
Model IV ($X1$ and $X3$)	$\chi^2=1.66$	$\chi^2=1.50$	$\chi^2=1.25$
Model V ($X1$ and $X4$)	$\chi^2=2.04$	$\chi^2\sim3.2$	$\chi^2\sim1.5$
Model VI (anion-Frenkel)	$\underline{\chi^2=1.28}$	$\chi^2=1.47$	$\underline{\chi^2=1.13}$
Cations	Sr in 4(a) at 0,0,0, etc.	Sr in 4(a) at 0,0,0, etc.	Ba in 4(a) at 0,0,0, etc.
	$u_{Sr}=0.067(4)$	$u_{Sr}=0.104(2)$ Å^2	$u_{Ba}=0.12(1)$ Å^2
Anions	Cl1 in 8(c) at $\frac{1}{4},\frac{1}{4},\frac{1}{4}$, etc.	Br1 in 8(c) at $\frac{1}{4},\frac{1}{4},\frac{1}{4}$, etc.	Cl1 in 8(c) at $\frac{1}{4},\frac{1}{4},\frac{1}{4}$, etc.
	$u_{Cl1}=0.100(3)$ Å^2	$u_{Br1}=0.095(3)$ Å^2	$u_{Cl1}=0.101(9)$ Å^2
	$m_{Cl1}=6.3(2)$	$m_{Br1}=4.57(9)$	$m_{Cl1}=6.8(2)$
	Cl2 in 48(g) at $\frac{1}{2},y,y$, etc.	Br2 in 48(g) at $\frac{1}{2},y,y$, etc.	Cl2 in 48(g) at $\frac{1}{2},y,y$, etc.
	$y_{Cl2}=0.357(8)$	$y_{Br2}=0.331(2)$	$y_{Cl2}=0.37(1)$
	$u_{Cl2}=0.100(3)$ Å^2	$u_{Br2}=0.23(1)$ Å^2	$u_{Cl2}=0.12(2)$ Å^2
	$m_{Cl2}=0.6(2)$	$m_{Br1}=3.43(9)$	$m_{Cl2}=0.4(2)$
	Cl3 in 32(f) at x,x,x, etc.	–	Cl3 in 32(f) at x,x,x, etc.
	$x_{Cl3}=0.39(1)$		$x_{Cl3}=0.40(2)$
	$u_{Cl3}=0.100(3)$ Å^2		$u_{Cl3}=0.12(2)$ Å^2
	$m_{Cl3}=1.1(2)$		$m_{Cl3}=0.8(2)$
Weighted profile R-factor (%)	$R_{wp}=0.73$	$R_{wp}=0.45$	$R_{wp}=1.38$
Expected R-factor (%)	$R_{exp}=0.65$	$R_{exp}=0.40$	$R_{exp}=1.30$
Number of data points	$N_d=3584$	$N_d=2735$	$N_d=3179$
Number of fitted params.	$N_v=27$	$N_v=26$	$N_v=27$

The anion site occupancies, m, are defined such that the total is that given by the stoichiometry (eight). The weighted profile and expected R-factors are given by

$$R_{wp}^2 = \sum_{N_d}\frac{(I_{obs}-I_{calc})^2}{(\sigma I_{obs})^2}\bigg/\sum_{N_d}\frac{(I_{obs})^2}{(\sigma I_{obs})^2} \text{ and } R_{exp}^2 = (N_d-N_v)\bigg/\sum_{N_d}\frac{(I_{obs})^2}{(\sigma I_{obs})^2}$$

(such that $\chi^2 = R_{wp}^2/R_{exp}^2$, see Eq. (1)) and the summations are made over the N_d data points used in the fit. N_v is the number of fitted variables. I_{obs} and I_{calc} are the observed and calculated intensities, respectively, and σI_{obs} is the estimated standard deviation on I_{obs}. The values of χ^2 obtained by fitting different structural models are listed, where values in italics indicate an unstable refinement or unphysical results and the value obtained for the best model is underlined.

value for α-SrBr$_2$ under ambient conditions of 0.61448(1) implies a slight compression along the [0 0 1] axis.

The cubic fluorite structure is characterised by an f.c.c. sublattice of cations and the equivalent positions within the α-SrBr$_2$ structure comprise the 8(g) general x,y,z positions with $x=0.15$, $y=0.55$ and $z=0.25$, plus the 2(c) $\frac{1}{4}\frac{1}{4}z$ sites with $z=0.75$. These sites correspond to the Sr1 and Sr2 positions in the α-SrBr$_2$ structure though, with reference to Table 2, both are shifted by ~0.7 Å from their ideal sites (in roughly [0 0 1] and [1 0 0] directions of the tetragonal cell). The effect of these displacements is to vary the 12 nearest neighbour Sr^{2+}–Sr^{2+} distances, which then span the range from ≈4.60 Å to ≈6.04 Å.

Within an f.c.c. sublattice there are two tetrahedral interstices and one octahedral interstice per lattice ion. In the case of an ideal α-SrBr$_2$ arrangement, the former comprise two general 8(g) sites with $x=0.05$, $y=0.35$, $z=0.50$ and $x=0.35$, $y=0.45$, $z=0.00$, plus the 2(a) $\frac{1}{4},\frac{3}{4},\frac{1}{2}$ and 2(b) $\frac{1}{4},\frac{3}{4},\frac{1}{2}$ sites, whilst the latter are formed by 8(g) sites with $x=0.05$, $y=0.85$, $z=0.25$ plus 2(c) $\frac{1}{4},\frac{1}{4},z$ sites with $z=0.25$. The fluorite structure is formed by filling all the tetrahedral interstices and leaving all the octahedral holes empty and this is also the case for the α-SrBr$_2$ arrangement. Thus, the ideal sites given above correspond to the Br1, Br2, Br3 and Br4 positions, respectively. The latter two are special positions of space group $P4/n$ and, as discussed in the previous subsection, their surrounding cation co-ordination is very close to tetrahedral. However, the Br1 and Br2 positions in α-SrBr$_2$ are

significantly shifted from their ideal sites (by ~2.0 Å in approximately [0 0 1]$_\alpha$ and ~0.7 Å in roughly [1 1 1]$_\alpha$, see Fig. 8b), which converts the corner-sharing array of SrBr$_8$ cubes in the fluorite structure into the face-sharing arrangement of distorted SrBr$_8$ square antiprisms in α-SrBr$_2$.

The structural description of α-SrBr$_2$ derived at 291(1) K was used as the starting model for the analysis of the diffraction data collected at the first temperature on heating (371(1) K) and this process continued iteratively to perform a detailed study of the evolution of the tetragonal structure with temperature. These results are listed in the supplementary material (Suppl. 3 and Suppl. 4). Considering the positional parameters, x_{Sr1} increases and y_{Sr1}, z_{Sr1}, z_{Sr2}, x_{Br1}, z_{Br1}, y_{Br2} and z_{Br2} decrease with temperature, whilst y_{Br1} and x_{Br2} show relatively little change. With the exception of z_{Sr1}, these trends are broadly consistent with a tendency towards the fluorite structure, though the α-SrBr$_2$ phase still shows significant displacements of both the cations and anions away from the idealised fluorite positions, even at the highest temperature of 912(1) K.

3.4. Superionic phase β-SrBr$_2$

At a temperature of 912(1) K evidence of additional reflections appeared at d-spacings of ~2.27 Å and ~2.66 Å. The temperature was increased slowly to 917(1) K, 920(1) K, 922(1) K and then 924(1) K, as the peaks from the new phase increased in intensity

at the expense of the those due to the low temperature (tetragonal) phase of α-SrBr$_2$. At each temperature step, a sequence of short ($\sim$5 min) data collections was performed to monitor the progress of the phase transition. After an initial increase in the quantity of the new phase on heating, no further changes were observed after around 30 min. Based on a crude observation of the peak intensities, the fraction of the new phase was estimated to reach $\sim$20%, $\sim$45%, $\sim$60% and $\sim$85% at the four temperatures.
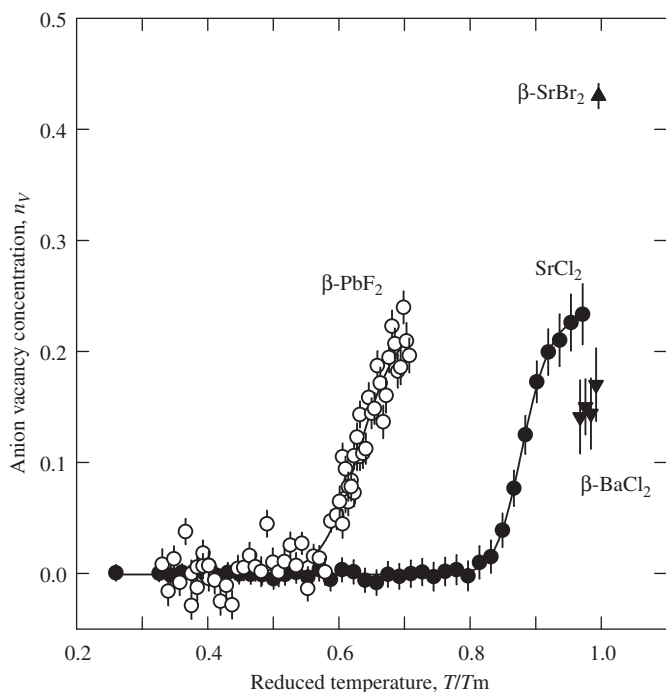
Fig. 4. The temperature dependence of the anion vacancy concentration within the fluorite-structured halide superionics SrCl$_2$ (●), β-SrBr$_2$ (▲), β-BaCl$_2$ (▼) and β-PbF$_2$ (○). The superionic transition temperatures are $\approx$1001 K, 920(3) K, 917(5) K and $\approx$711 K, respectively. To allow comparison between different compounds, the x-axis is shown in the form T/T_m, where T_m is the melting temperature. The data for SrCl$_2$, β-SrBr$_2$ and β-BaCl$_2$ are obtained in this work, whilst that for β-PbF$_2$ is published in reference [34].
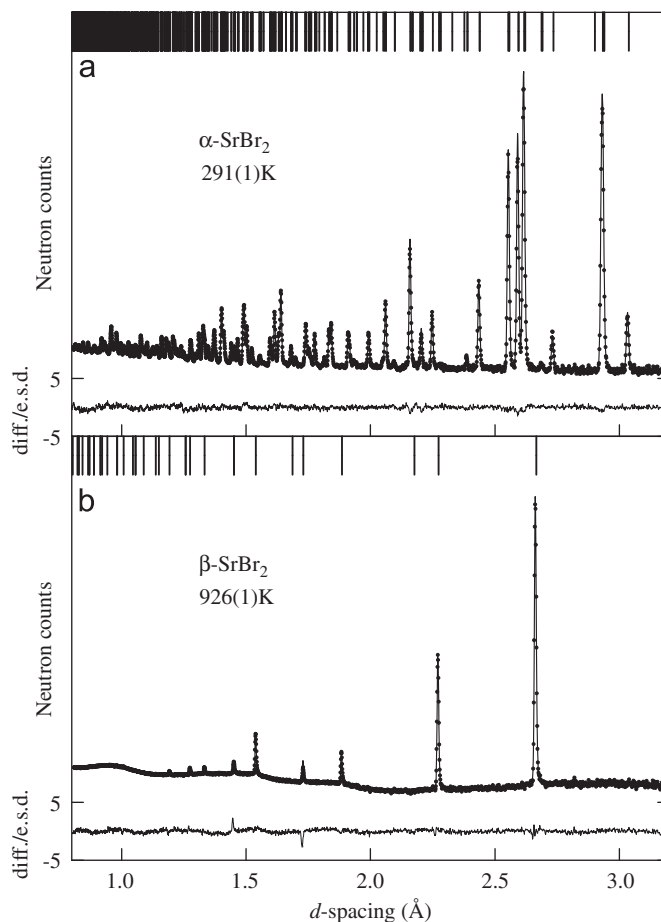
Fig. 6. The least-squares fits to the powder neutron diffraction data collected from (a) α-SrBr$_2$ at 291(1) K and (b) β-SrBr$_2$ at 926(1) K. The dots are the experimental data points (with the background from the silica sample container and furnace subtracted) and the solid lines are the calculated profiles using the parameters listed in Tables 2 and 1, respectively. The lower traces show the difference (measured minus calculated) divided by the estimated standard deviation on the experimental data points. The rows of tick marks along the top of the figures denote the calculated positions of all the symmetry allowed Bragg reflections for space groups $P4/n$ (α-SrBr$_2$) and $Fm\bar{3}m$ (β-SrBr$_2$).
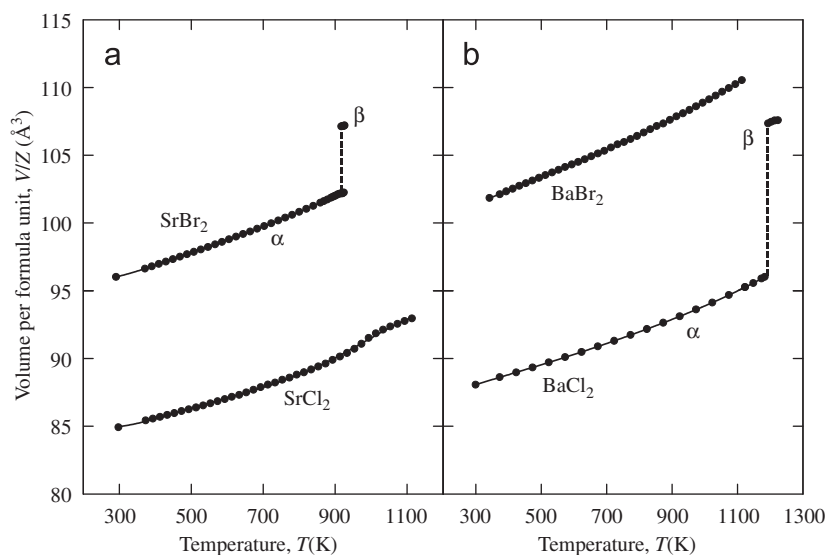
Fig. 5. The temperature dependence of the unit cell volume per formula unit, V/Z, for (a) SrCl$_2$ and SrBr$_2$ and (b) BaCl$_2$ and BaBr$_2$.

Table 2

Summary of the results of the least-squares refinements of the neutron powder diffraction data collected from α-SrBr$_2$, α-BaCl$_2$ and BaBr$_2$ at temperatures close to ambient.

| Phase	α-SrBr$_2$	α-BaCl$_2$	BaBr$_2$
Temperature (K)	$T=291(1)$	$T=299(1)$	$T=342(1)$
Space group	$P4/n$	$Pnma$	$Pnma$
Lattice parameters (Å)	$a=11.6042(1)$	$a=7.8813(2)$	$a=8.2746(1)$
	$c=7.1306(1)$	$b=4.7369(1)$	$b=4.9599(1)$
		$c=9.4360(2)$	$c=9.9264(2)$
Unit cell volume (Å^3)	$V=960.18(2)$	$V=352.27(1)$	$V=407.40(1)$
Volume per formula unit (Å^3)	$V/Z=96.018(2)$	$V/Z=88.068(2)$	$V/Z=101.849(3)$
Cations	Sr1 in 8(g) at x,y,z, etc.	Ba in 4(c) at $x_{Ba},\frac{1}{4},z_{Ba}$, etc.	Ba in 4(c) at $x_{Ba},\frac{1}{4},z_{Ba}$, etc.
	$x_{Sr1}=0.1057(1)$	$x_{Ba}=0.2495(5)$	$x_{Ba}=0.2491(3)$
	$y_{Sr1}=0.5855(1)$	$z_{Ba}=0.1170(3)$	$z_{Ba}=0.1179(2)$
	$z_{Sr1}=0.2491(4)$	$u_{Ba}=0.0191(7)$ Å^2	$u_{Ba}=0.0151(4)$ Å^2
	$u_{Sr1}=0.0068(3)$ Å^2		
	Sr2 in 2(c) at $\frac{1}{4},\frac{1}{4},z$, etc.	–	–
	$z_{Sr2}=0.8529(5)$		
	$u_{Sr2}=0.0050(6)$ Å^2		
Anions	Br1 in 8(g) at x,y,z, etc.	Cl1 in 4(c) at $x_{Cl1},\frac{1}{4},z_{Cl1}$, etc.	Br1 in 4(c) at $x_{Br1},\frac{1}{4},z_{Br1}$, etc.
	$x_{Br1}=0.1531(2)$	$x_{Cl1}=0.1443(2)$	$x_{Br1}=0.1431(2)$
	$y_{Br1}=0.4589(3)$	$z_{Cl1}=0.4293(2)$	$z_{Br1}=0.4299(2)$
	$z_{Br1}=0.6229(3)$	$u_{Cl1}=0.0198(4)$ Å^2	$u_{Br1}=0.0171(4)$ Å^2
	$u_{Br1}=0.0152(5)$ Å^2		
	Br2 in 8(g) at x,y,z, etc.	Cl2 in 4(c) at $x_{Cl2},\frac{1}{4},z_{Cl2}$, etc.	Br2 in 4(c) at $x_{Br2},\frac{1}{4},z_{Br2}$, etc.
	$x_{Br2}=0.3389(2)$	$x_{Cl2}=0.0295(3)$	$x_{Br2}=0.0287(2)$
	$y_{Br2}=0.4580(2)$	$z_{Cl2}=0.8291(2)$	$z_{Br2}=0.8293(2)$
	$z_{Br2}=0.0996(3)$	$u_{Cl2}=0.0253(5)$ Å^2	$u_{Br2}=0.0234(4)$ Å^2
	$u_{Br2}=0.0090(5)$ Å^2		
	Br3 in 2(a) at $\frac{1}{4},\frac{3}{4},0$, etc.	–	–
	$u_{Sr2}=0.0072(9)$ Å^2		
	Br4 in 2(b) at $\frac{1}{4},\frac{3}{4},\frac{1}{2}$, etc.	–	–
	$u_{Sr2}=0.0093(9)$ Å^2		
Weighted profile R-factor (%)	$R_{wp}=1.47$	$R_{wp}=1.43$	$R_{wp}=1.78$
Expected R-factor (%)	$R_{exp}=1.31$	$R_{exp}=1.35$	$R_{exp}=1.62$
Number of data points	$N_d=3180$	$N_d=3179$	$N_d=3008$
Number of fitted params.	$N_v=33$	$N_v=27$	$N_v=27$

The weighted profile and expected R-factors are given by

$$R_{wp}^2 = \sum_{N_d} \frac{(I_{obs}-I_{calc})^2}{(\sigma I_{obs})^2} \bigg/ \sum_{N_d} \frac{(I_{obs})^2}{(\sigma I_{obs})^2} \text{ and } R_{exp}^2 = (N_d - N_v) \bigg/ \sum_{N_d} \frac{(I_{obs})^2}{(\sigma I_{obs})^2}$$

(such that $\chi^2 = R_{wp}^2/R_{exp}^2$, see equation (1)) and the summations are made over the N_d data points used in the fit. N_v is the number of fitted variables. I_{obs} and I_{calc} are the observed and calculated intensities, respectively, and σI_{obs} is the estimated standard deviation on I_{obs}.

Table 3

The Sr–Br bond lengths and Br–Sr–Br bond angles in α-SrBr$_2$ at 291(1) K.

Sr1	Sr1–Br1: 3.093(4) Å; 3.181(3)Å; 3.597(3) Å	Br1–Sr1–Br1: 67.5(1)°; 81.00(9)°; 105.44(9)°
	Sr1–Br2: 3.143(3) Å; 3.145(3)Å; 3.263(3) Å	Br1–Sr1–Br2: 72.96(6)°; 74.20(5)°; 75.95(7)°; 85.35(7)°; 84.35(8)°; 138.0(1)°
	Sr1–Br3: 3.099(2) Å	143.43(9)°; 149.12(6)°; 155.61(7)°
	Sr1–Br4: 3.106(2) Å	Br1–Sr1–Br3: 83.21(6)°; 133.69(7)°; 140.74(8)°
		Br1–Sr1–Br4: 65.86(6)°; 72.54(8)°; 116.32(9)°
		Br2–Sr1–Br2: 70.79(9)°; 81.81(8)°; 108.7(1)°
		Br2–Sr1–Br3: 69.15(6)°; 70.69(7)°; 119.6(1)°
		Br2–Sr1–Br4: 91.15(5)°; 125.28(7)°; 151.89(8)°
		Br3–Sr1–Br4: 70.15(3)°
Sr2	Sr2–Br1: 3.135(3) Å × 4	Br1–Sr2–Br1: 74.13(7)° × 4; 116.9(1)° × 2
	Sr2–Br2: 3.160(3) Å × 4	Br1–Sr2–Br2: 76.40(5)° × 4; 79.49(4)° × 4; 139.88(4)° × 4; 144.84(4)° × 4
		Br2–Sr2–Br2: 71.94(7)° × 4; 112.3(1)° × 2
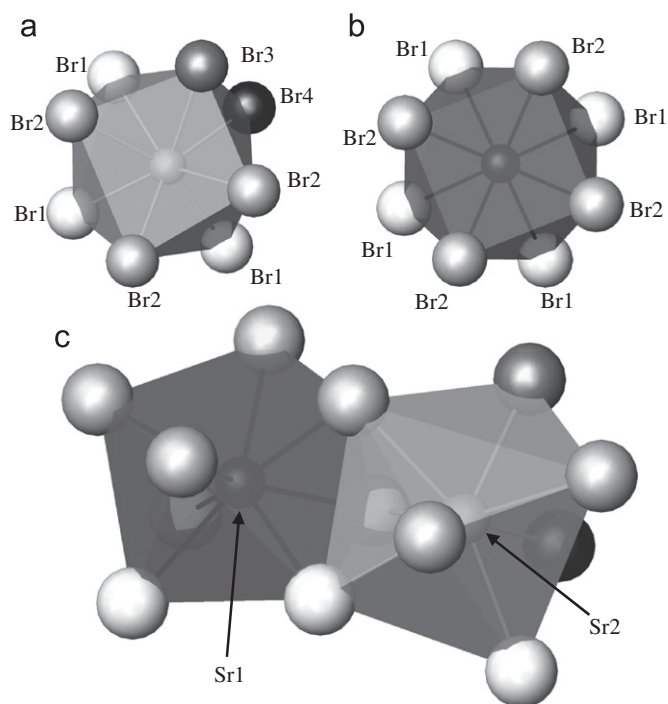
Fig. 7. The anion environment surrounding the (a) Sr1 and (b) Sr2 cations in α-SrBr$_2$. (c) The Sr1Br$_8$ and Sr2Br$_8$ square antiprisms are linked by common triangular faces.
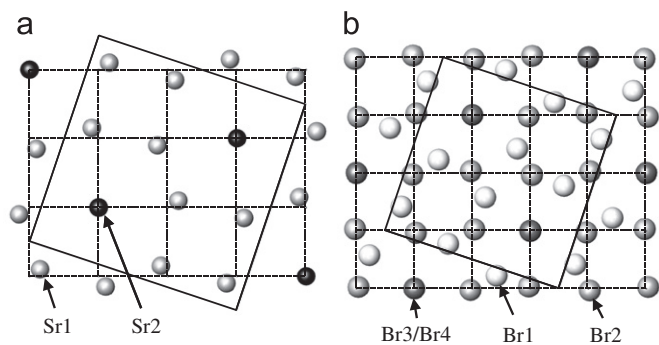
Fig. 8. The relationship between the unit cell of α-SrBr$_2$ (solid line) and (a) the cation sublattice and (b) the anion sublattice of the fluorite structure (dashed lines), projected down the [0 0 1] tetragonal axis of the former. The cations within α-SrBr$_2$ are slightly displaced from the fluorite positions (at the intersections of the dashed lines), whilst more extensive displacements occur within the anion sublattice.

No peaks from the α phase could be observed on further heating to 926(1) K, and the transition was deemed to be complete. The structural change appears to be associated with the transition observed in DSC measurements [22,28,29] and the marked increase in the ionic conductivity of SrBr$_2$ [20] at temperatures of around 920 K.

The neutron powder diffraction pattern collected from the β phase of SrBr$_2$ at 926(1) K was considerably simpler than that obtained for α-SrBr$_2$, with the strongest Bragg peaks observed at d-spacings of approximately 1.54 Å, 1.73 Å, 1.89 Å, 2.27 Å and 2.67 Å. These reflections, together with two further peaks observed at around 3.77 Å and 4.35 Å in detectors at lower scattering angles (albeit with lower $\Delta d/d$ resolution), are consistent with an f.c.c. lattice with $a \approx 7.54$ Å (in increasing order of d-spacing, they correspond to the 4 2 2, 3 3 1, 4 0 0, 3 1 1, 2 2 0, 2 0 0 and 1 1 1 reflections). This assignment implies that the β-SrBr$_2$ phase adopts the cubic fluorite crystal structure, as

observed for SrCl$_2$ and several other fluorides under ambient conditions [15]. However, attempts to fit the diffraction data using model I, with an ideal cubic fluorite structure produced a relatively poor quality-of-fit, with $\chi^2 = 5.37$.

The high ionic conductivity reported for β-SrBr$_2$ [20] and the relative magnitudes of the enthalpies of the α→β and melting transitions [22] indicates the presence of extensive dynamic disorder within the crystalline lattice. By analogy with SrCl$_2$ (Section 3.1) and the other fluorite-structured superionics (see [1–8]), it is reasonable to assume that the disorder predominantly occurs within the anion sublattice. This view is supported by the reduction in the mean occupancy of the Br$^-$ site (to ~0.69) when this parameter is allowed to vary within the fitting procedure (model II). However, following the same procedure adopted for superionic SrCl$_2$ in Section 3.1, this simple model is physically unrealistic and it is necessary to consider the locations of the displaced anions.

The structural model (model III) allowing the anions to be distributed over the Br1 and Br2 sites and provided a stable refinement with an excellent fit to the experimental data ($\chi^2 = 1.28$) and physically sensible values for both the site occupancies and thermal vibration parameters. By contrast, using the Br1 and Br3 sites (model IV) gave a somewhat poorer fit ($\chi^2 = 1.50$) which diverged when attempting to vary the single positional parameter x_{Br3}. Including both the Br2 and Br3 sites in model VI, but constraining their occupancies to be in the ratio 1:2 in order to model the anion-Frenkel defects illustrated in Fig. 2c, gave a similar quality-of-fit to the data, but converged to a physically meaningless model in which the occupancy of the lattice Br1 sites had a significant negative value. Finally, in the case of the Br4 sites (model V), a relatively high χ^2 of ~3.2 was obtained, which was both unstable (unless the thermal parameters associated with the Br1 and Br4 positions were constrained to be equal) and gave a negative occupancy for the Br4 site. As a result, we conclude that the best fit to the neutron powder diffraction data collected from β-SrBr$_2$ at 926(1) K is obtained with structural model III in which the anions are distributed over the Br1 and Br2 sites shown in Fig. 2b. The quality of the final fit to the experimental data is illustrated in Fig. 6b and the resultant fitted parameters are listed in Table 1. This time-averaged structure of β-SrBr$_2$ can be described as a disordered-fluorite arrangement, with the anions located on the Br2 sites representing some form of interstitial site associated with the extensive Br$^-$ disorder. However, the distance between the (lattice) Br1 and Br2 positions is only ~2.8 Å, which is significantly smaller than twice the ionic radius of Br$^-$ (2×1.96 Å = 3.92 Å [36]). As a result, two neighbouring sites cannot be simultaneously occupied. In the superionic phases of the other fluorite-structured halides, the two lattice anions closest to the interstitial relax away in ⟨1 1 1⟩ directions to avoid such contacts (see Fig. 1c), but the absence of any significant occupancy of the $X3$ sites does not support the formation of such defect clusters within the β-SrBr$_2$ phase.

An alternative structural model involving anion occupancy of the $X2$ sites within the fluorite structure without anomalously short anion–anion distances has been proposed for the case of anion-excess fluorites [37]. As illustrated in Fig. 9, the conversion of an SrBr$_8$ cube into an SrBr$_8$ square antiprism involves the rotation of one of the square faces by 45°. If all the Br$^-$–Br$^-$ distances are equal, the four anions comprising the twisted face occupy Br2 sites, with a value of $y_{Br2} = \sqrt{1/8} = 0.354$ given by simple geometric considerations [38,39]. The similarity between this value and that given by the analysis of the neutron powder diffraction data collected from β-SrBr$_2$ ($y_{Br2} = 0.331(2)$) suggests that such structural units might be present within this superionic phase. Additional support for this local environment around the
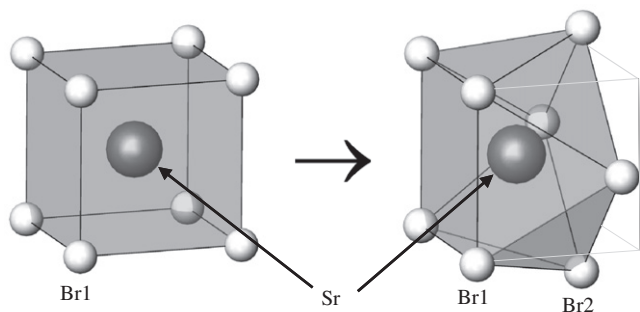
Fig. 9. Schematic diagram illustrating the conversion of an $SrBr_8$ cube into an ideal $SrBr_8$ square antiprism by rotation of one of the square faces by 45°.

Sr^{2+} within the (disordered) β phase of $SrBr_2$ is provided by the presence of square antiprisms in the (long-range ordered) structure of α-$SrBr_2$ (see Section 3.2). Furthermore, the conversion of the anion sublattice shown in Fig. 9 might be expected to result in coupled displacements of the central cation in $\langle 1\,0\,0\,0 \rangle$ directions by around 0.3 Å (so that the Sr^{2+} remains close to the centre of its anion polyhedron), which would explain the relatively high isotropic cation thermal vibration parameter u_{Sr} within the β phase of $SrBr_2$ (Table 1).

3.5. Crystal structure of α-$BaCl_2$ and $BaBr_2$

Under ambient conditions, both $BaCl_2$ and $BaBr_2$ adopt the cotunnite crystal structure in space group $Pnma$ [40], with the Ba^{2+} cations and two, symmetry independent, anions, Cl1/Br1 and Cl2/Br2, all located in $4(c)$ sites at $x,\frac{1}{4},z$, etc. A detailed analysis of the crystal structures of $BaCl_2$ and $BaBr_2$ using neutron powder diffraction was performed using data collected at temperatures of 299(1) K and 342(1) K, respectively. In both the cases, all the observed Bragg peaks could be indexed on the basis of an orthorhombic unit cell (with $a \sim 7.88$ Å, $b \sim 4.73$ Å and $c \sim 9.44$ Å for $BaCl_2$ and $a \sim 8.27$ Å, $b \sim 4.95$ Å and $c \sim 9.93$ Å for $BaBr_2$) and with extinction conditions ($0\,k\,l$, $k+l=2n$; $h\,k\,0$, $h=2n$; $h\,0\,0$, $h=2n$; $0\,k\,0$, $k=2n$; $0\,0\,l$, $l=2n$) consistent with $Pnma$ symmetry. Rietveld refinement of the diffraction data used the published positional parameters for both compounds [40], with good fits obtained in both cases ($\chi^2=1.13$ and $\chi^2=1.21$, for $BaCl_2$ and $BaBr_2$, respectively). A total of 27 variable parameters were used in the final fitting procedure, comprising a scale factor, three lattice parameters, 6 positional parameters (x_{Ba}, z_{Ba}, $x_{Cl1/Br1}$, $z_{Cl1/Br1}$, $x_{Cl2/Br2}$ and $z_{Cl2/Br2}$), three isotropic thermal vibration parameters (u_{Ba}, $u_{Cl1/Br1}$, and $u_{Cl2/Br2}$), four parameters describing Gaussian and Lorentzian contributions to the instrumental peak-shape and 10 coefficients of a shifted Chebyshev polynomial function used to describe the background scattering. The final fitted values are listed in Table 2, together with details of the goodness-of-fit parameters. For both compounds, the structural parameters given in Table 2 are in good agreement with those published previously though, as expected, the new results have smaller estimated standard deviations. Refinements using aniso-tropic thermal vibrations for the ions gave no significant improvements in the quality of the fits and are not reported here.

As illustrated in Fig. 2d, the anion co-ordination around the Ba^{2+} comprises a trigonal pyramid (constructed from two Cl1/Br1 and four Cl2/Br2) with three additional anions (two Cl1/Br1 and one Cl2/Br2) located outside each of the rectangular faces. However, this ninefold anion environment around the Ba^{2+} is rather distorted, with distances of 3.061(4) Å, 3.074(3) Å ($\times 2$), 3.142(4) Å, 3.223(4) Å, 3.272(3) Å ($\times 2$) and 3.557(3) Å ($\times 2$) for $BaCl_2$ at 299(1) K (3.219(3) Å, 3.230(2) Å ($\times 2$), 3.294(3) Å, 3.396(3) Å, 3.422(2) Å ($\times 2$) and

3.733(2) Å ($\times 2$) for $BaBr_2$ at 342(1) K). With increasing temperature, x_{Cl1} and x_{Br1} show a slightly increasing trend, with little significant change in the other positional parameters (see supplementary material, Suppl. 5 and Suppl. 6) resulting in no marked change in the nature of the anion co-ordination around the Ba^{2+}. No evidence of anion disorder was observed in either compound at the highest temperatures, with refinements of the site occupancies of the two anion positions yielding values of unity, within the estimated standard deviation. This is consistent with the situation reported for the cotunnite-structured α phase of PbF_2 when heated at elevated pressures [19], but contrary to the increased ionic conductivity observed in cotunnite-structured $PbCl_2$ as its temperature approaches the melting point [21]. Whilst the cotunnite-structured phase of $BaBr_2$ is stable up to the melting point of 1130 K, a phase transition has been reported to occur in $BaCl_2$ at temperatures around 1193 K on the basis of ionic conductivity measurements [20] and thermal analysis methods [22], prior to melting at 1233 K. The presence of the phase transition in $BaCl_2$ is confirmed in this work by a complete change in the neutron powder diffraction patterns collected at temperatures of 1183(1) K and 1193(1) K. The structural properties of the high temperature phase, which we label β, are considered in the following subsection using neutron powder diffraction data collected at 1203(1) K.

3.6. Superionic phase β-$BaCl_2$

The neutron powder diffraction pattern collected from the β phase of $BaCl_2$ at 1203(1) K showed Bragg peaks at d-spacings of approximately 1.54 Å, 1.73 Å, 1.89 Å, 2.27 Å, 2.67 Å, 3.77 Å and 4.36 Å which are consistent with an f.c.c. lattice with $a \approx 7.54$ Å. This assignment is, coincidentally, the same as for β-$SrBr_2$ discussed in Section 3.4, and indicates that the β-$BaCl_2$ phase adopts the cubic fluorite crystal structure. By analogy with other binary halides, the presence of a fluorite-structured phase in $BaCl_2$ at elevated temperatures is not particularly surprising and has, indeed, been implied by observations of a phase with this ionic arrangement within thin films of $BaCl_2$ [41], in $BaCl_2$ doped with $EuCl_2$ [42] and in dehydration products of $BaCl_2 \cdot nH_2O$ [40,43].

As in the case of β-$SrBr_2$, the high ionic conductivity reported for β-$BaCl_2$ [20] and the relative magnitudes of the enthalpies of the α→β and melting transitions [22] indicates the presence of extensive dynamic disorder within the fluorite lattice. This is confirmed by the relatively poor fit the diffraction data obtained using model I (the ideal cubic fluorite structure), with $\chi^2=2.17$. The presence of significant anion disorder is highlighted by the significant reduction in χ^2 (to 1.66) when using model II, with a reduction in the mean occupancy of the Cl$^-$ site to ~ 0.70. Models III and IV, which constrain the displaced anions to occupy the Cl2 and Cl3 sites, respectively, both gave improved fits (see Table 1) with stable refinements if the isotropic thermal vibration parameters of the two anion sites were constrained to remain equal. It was not possible to obtain a stable structural refinement using the Cl4 sites (model V). The final structural model (model VI), which includes the possibility of dynamic anion-Frenkel defects of the kind illustrated in Fig. 2c, gave the best fit to the data, with $\chi^2=1.13$ (see Fig. 3b) and the fitted parameters listed in Table 1. On this basis, the superionic phase of β-$BaCl_2$ resembles that found in $SrCl_2$ (see Section 3.1) and other fluorite-structured compounds (such as CaF_2 and β-PbF_2 [11]), rather than that reported here for β-$SrBr_2$ (Section 3.4).

3.7. Fluorite-structured superionic phases

Following the work presented in this paper, it is possible to list six fluorite-structured, AX_2 alkaline-earth halides which show

superionic conduction at elevated temperatures, namely CaF_2, SrF_2, BaF_2, $SrCl_2$, β-$BaCl_2$ and β-$SrBr_2$ [4,7,44]. The first four all undergo gradual transitions to the superionic state (classified as a type-II transition in the notation of Boyce and Huberman [44]), with the onset of the high ionic conductivity associated with a maximum in the specific heat, C_p, (which has been used to define superionic transition temperatures of 1430 K, 1400 K, 1275 K and 1001 K in CaF_2, SrF_2, BaF_2 and $SrCl_2$, respectively, see [7] and references therein) and anomalies in the thermal expansion (see [33–35] and the example of $SrCl_2$ shown in Fig. 5a). By contrast, $BaCl_2$ and $SrBr_2$ reach the superionic phase via a first-order ($\alpha \rightarrow \beta$) structural phase transition (a type-I transition [44]), with abrupt increases in the ionic conductivity of several orders of magnitude (see Fig. 1 [20]) and large discontinuities in the volume per formula unit, V/Z (see Fig. 5). A number of attempts to 'predict' the type-I/type-II nature of the superionic transition in model compounds have been made, including the work of Hainovsky and Maier based on the inclusion of an additional term in the free enthalpy of the disordered crystal with a cube-root dependence on the defect concentration, n [45]. However, merit of this approach has been questioned by other authors [46].

In addition to the alkaline-earth based compounds, β-PbF_2 is a fluorite-structured halide compound which undergoes a type-II superionic transition on heating [1–3,47]. However, its superionic transition occurs at a relatively low temperature of 711 K [1], even when scaled to the melting temperature. The latter is demonstrated in Fig. 4 by the comparison of the fraction of anions leaving the lattice sites, n_V, (as determined by diffraction studies) for β-PbF_2 [34] and $SrCl_2$ (this work) and has been attributed to cation polarisation effects which are a consequence of the electronic configuration of the Pb^{2+} species [48,49]. Nevertheless, detailed neutron diffraction studies using single crystal samples concluded that the superionic phase of β-PbF_2 is characterised by the same thermally-induced anion-Frenkel defects (shown in Fig. 2c) as CaF_2 and $SrCl_2$. However, the presence of these defects causes extensive relaxations of the surrounding anion sublattice, whose extent increases as the effective size of the X^- anions increases (such that the ratio of the ionic sizes, r_X/r_A, increases from 1.02 for β-PbF_2 to 1.17 for CaF_2 and 1.44 for $SrCl_2$ [36]) [11]. Indeed, at the other extreme, such relaxations are virtually absent in the case of antifluorite-structured superionics such as Li_2O [50], since it is the smaller ionic species which is mobile (such that the corresponding ratio is r_A/r_X has a value of only 0.43 for Li_2O [36]). In the case of β-$SrBr_2$ ($r_X/r_A = 1.56$ [36]), it is probable that the large size of the Br^- ion requires relaxations to occur over such large distances as to be energetically unfavourable and alternative defect structures, such as that illustrated in Fig. 9, are adopted instead. When comparing the extent of ionic disorder between different compounds using data obtained by diffraction methods, such as that shown in Fig. 4, it is important to note that the number of anions leaving the regular lattice sites differs from the number of thermally induced defects, either because the former includes both true interstitials and neighbouring anions relaxed off their regular lattice sites (so that, for example, there would be a factor of 3 for the Frenkel defects illustrated in Fig. 2c) or because the defects comprise several interstitials (i.e. there would be a factor of 4 for the square antiprism defect shown in Fig. 9). In the past, such issues have proved troublesome when comparing the defect concentrations with fluorite-structured superionics obtained by diffraction [9,11,51] and computer simulation [52,53] approaches. Irrespective of such issues, the extent of the dynamic disorder within the superionic phase of the fluorite-structured halides means that simple models of isolated defect clusters of the type shown in Fig. 2c or Fig. 9 are a simplification of the true picture, with extensive interactions between different

defects likely within the real material. Such effects are likely to be the cause of the levelling of the both the concentrations of anions leaving the lattice sites (see Fig. 4 for the case of $SrCl_2$) and the ionic conductivity [1–3,5].

4. Conclusions

Interest in the structure–property relationships within the fluorite-structured, AX_2 alkaline-earth halides primarily focuses on the nature of structural disorder and the (super)ionic conductivity. A comparative study of the ionic conductivities, σ, (after correction for the effects of differing ionic densities) showed that σ increases in the sequence $SrCl_2 \rightarrow CaF_2 \rightarrow SrF_2 \rightarrow BaF_2$, whilst the abrupt increase in σ at the melting transition becomes smaller [8]. Since the ratio of the ionic sizes, r_A/r_X, increases along this series, it was suggested that an increase in the relative size of the anion interstitial sites increases the extent of disorder, which is consistent with the trend observed in the activation energies for Frenkel defect formation [54]. However, as highlighted by the simplest expression for the ionic conductivity, $\sigma = n\mu q$ (where n, μ and q are the number, mobility and charge of the mobile defects, respectively), it is necessary to consider both the concentration and dynamics of the ionic disorder.

As discussed in the previous subsection, the number of thermally induced defects is difficult to estimate with any degree of confidence. Turning to the ionic mobility, the superionic conduction process can be crudely described as the diffusion of one ionic species between interstices formed by a rigid sublattice of counterions. Hopping between individual sites requires the mobile ion to 'squeeze' through gaps formed by the array of immobile ions and, on these grounds, high ionic conductivity might be expected to be favoured in the case of small mobile ions. In the case of halide superionic conductors, the intuitive preference for smaller mobile species is supported by the observation of numerous superionic fluorides (for a review, see [7]). By contrast, there are only a few chlorine-ion conductors, such as $SrCl_2$ [3,8,20], $CH_3NH_3GeCl_3$ [55] and a small number of compounds containing Sn^{2+} and Pb^{2+} cations [56]. To the best of our knowledge, $SrBr_2$ is the only example of a bromine compound showing superionic behaviour at elevated temperature and, indeed, it is remarkable that such a large anion can show extensive diffusion through the cation sublattice. The presence of dynamic defect clusters of the type shown in Fig. 9 requires significant correlations between the motions of the Br^- in order to avoid anomalously short contacts. Whilst molecular dynamics simulations show extensive anion-anion correlations within the superionic phases of fluorite-structured halides [48,57], and the observation of significant diffuse scattering suggests their presence within the β-$SrBr_2$ phase (see Fig. 6b), it is not possible to obtain an unambiguous description of the nature of the short-range interactions between ions on the basis of analysis of the Bragg diffraction experiment alone. A detailed analysis of the diffuse scattering from the β-$SrBr_2$ phase (using the reverse Monte Carlo method), together with complementary computer simulations, is planned for the future.

Appendix A. Supplementary material

Supplementary data associated with this article can be found in the online version at doi:10.1016/j.jssc.2011.09.004.

References

[1] C.E. Derrington, M. O'Keeffe, Nat. Phys. Sci. 246 (1973) 44–46.
[2] R. Benz, Z. Phys. Chem. 95 (1975) 25–32.
[3] V.M. Carr, A.V. Chadwick, R. Saghafian, J. Phys. C: Solid State Phys. 11 (1978) L637–L641.
[4] W. Hayes, Contemp. Phys. 19 (1978) 469–486.
[5] C.E. Derrington, A. Lindner, M. O'Keeffe, J. Solid State Chem. 15 (1975) 171–174.
[6] A.V. Chadwick, Solid State Ionics 8 (1983) 209–220.
[7] S. Hull, Rep. Prog. Phys. 67 (2004) 1233–1314.
[8] B.M. Voronin, S.V. Volkov, J. Phys. Chem. Solids 62 (2001) 1349–1358.
[9] M.H. Dickens, W. Hayes, M.T. Hutchings, C. Smith, J. Phys. C: Solid State Phys. 12 (1979) L97–L102.
[10] S.M. Shapiro, F. Reidinger, Physics of superionic conductors, in: M.B. Salamon (Ed.), Topics in Current Physics, Springer-Verlag, Berlin, 1979.
[11] M.T. Hutchings, K. Clausen, M.H. Dickens, W. Hayes, J.K. Kjems, P.G. Schnabel, C. Smith, J. Phys. C: Solid State Phys. 17 (1984) 3903–3940.
[12] C.R.A. Catlow, W. Hayes, J. Phys. C: State Phys. 15 (1982) L9–L13.
[13] C.J. Howard, B.J. Kennedy, C. Curfs, Phys. Rev. B 72 (2005) art. 214114.
[14] B.J. Kennedy, C.J. Howard, Phys. Rev. B 70 (2004)art. 144102 70 (2004).
[15] R.W.G. Wyckoff, Crystal Structures, Krieger Publishing Company, Florida, 1982.
[16] J.M. Leger, J. Haines, A. Atouf, O. Schulte, S. Hull, Phys. Rev. B 52 (1995) 13247–13256.
[17] J. Oberschmidt, D. Lazarus, Phys. Rev. B 21 (1980) 2952–2961.
[18] G.A. Samara, J. Phys. Chem. Solids 40 (1979) 509–522.
[19] S. Hull, D.A. Keen, Phys. Rev. B 58 (1998) 14837–14844.
[20] C.E. Derrington, M. O'Keeffe, Solid State Commun. 15 (1974) 1175–1177.
[21] F.E.A. Melo, K.W. Garrett, J. Mendes Filho, J.E. Moreira, Solid State Commun. 31 (1979) 29–33.
[22] A.S. Dworkin, M.A. Bredig, J. Phys. Chem. 67 (1963) 697–698.
[23] M.A. Kamermans, Z. Kristall. 101 (1939) 406–411.
[24] R.L. Sass, T. Brackett, E. Brackett, J. Phys. Chem. 67 (1963) 2862–2863.
[25] J.G. Smeggil, H.A. Eick, Inorg. Chem. 10 (1971) 1458–1460.
[26] H.P. Beck, Angew. Chem. 83 (1971) 893–894.
[27] H. Beck, W. Dausch, J. Solid State Chem. 80 (1989) 32–39.
[28] R. Riccardi, C. Sinistri, G.V. Campari, A Magistri, Z. Natur. A 25 (1970) 781–785.
[29] K.H. Mahendran, K. Sujatha, R. Sridharan, T. Gnanasekaran, J. Alloys Comp. 358 (2003) 37–42.
[30] S. Hull, R.I. Smith, W.I.F. David, A.C. Hannon, J. Mayers, R. Cywinski, Physica B 180–181 (1992) 1000–1002.
[31] A.C. Larson, R.B. von Dreele, Los Alamos National Laboratory Report, (1994) LAUR 86-748.
[32] W. Schröter, J. Nölting, J. Phys. Coll. C6 (41) (1980) 20–23.
[33] T.S. Aurora, D.O. Pederson, S.M. Day, Phys. Rev. B 41 (1990) 9647–9649.
[34] J.P. Goff, W. Hayes, S. Hull, M.T. Hutchings, J. Phys.: CondensMatter 3 (1991) 3677–3687.
[35] R.B. Roberts, G.K. White, J. Phys. C: Solid. State Phys 19 (1986) 7167–7172.
[36] R.D. Shannon, Acta Cryst. A32 (1976) 751–767.
[37] J.P. Laval, B. Frit, J. Solid State Chem. 49 (1983) 237–246.
[38] D.J.M. Bevan, S.E. Lawton, Acta Cryst. B 42 (1986) 55–58.
[39] S. Hull, C.C. Wilson, J. Solid State Chem. 100 (1992) 101–114.
[40] E.B. Brackett, T.E. Brackett, R.L. Sass, J. Phys. Chem. 67 (1963) 2132–2135.
[41] B.K. Vainshtein, Doklady Akad. Nauk. SSSR 60 (1948) 1169–1172.
[42] L.H. Brixner, A. Ferretti, J. Solid State Chem. 18 (1976) 111–116.
[43] A. Haase, G. Brauer, Z. Anorg. Allg. Chem. 441 (1978) 181–195.
[44] J.B. Boyce, B.A. Huberman, Phys. Rep. 51 (1979) 189–265.
[45] N. Hainovsky, J. Maier, Phys. Rev. B 51 (1995) 15789–15797.
[46] A. Gray-Weale, P.A. Madden, J. Phys. Chem. B 108 (2004) 6624–6633.
[47] M. Faraday, Phil. Trans. R. Soc. (1838) 90.
[48] M.J. Castiglione, P.A. Madden, J. Phys.: Condens. Matter 13 (2001) 9963–9983.
[49] M.J. Castiglione, M. Wilson, P.A. Madden, J. Phys.: Condens. Matter 11 (1999) 9009–9024.
[50] T.W.D. Farley, W. Hayes, S. Hull, M.T. Hutchings, M. Vrtis, J. Phys.: Condens. Matter 3 (1991) 4761–4781.
[51] M.H. Dickens, W. Hayes, M.T. Hutchings, C. Smith, J. Phys. C: Solid State Phys. 15 (1982) 4043–4060.
[52] M.J. Gillan, M. Dixon, J. Phys. C: Solid State Phys. 13 (1980) 1901–1917.
[53] A.B. Walker, M. Dixon, M.J. Gillan, J. Phys. C: Solid State Phys. 15 (1982) 4061–4073.
[54] C.R.A. Catlow, M.J. Norgett, J. Phys. C: Solid State Phys. 6 (1973) 1325–1339.
[55] K. Yamada, K. Mikawa, T. Okuda, K.S. Knight, J. Chem. Soc. Dalton Trans. (2002) 2112–2118.
[56] I.V. Murin, O.V. Glumov, N.A. Mel'nikova, Russ. J. Electrochem 45 (2009) 411–416.
[57] A. Gray-Weale, P.A. Madden, J. Phys. Chem. B 108 (2004) 6634–6642.